Dynamic analysis of multi-crack problems by the spline fictitious boundary element method based on Erdogan fundamental solutions

Xu Zhi[a]

Chen Miao[a]

Su Cheng[a, b, *]

cvchsu@scut.edu.cn

Fan Xueming[a, b]

Guan Zhongwei[a, c]

[a]School of Civil Engineering and Transportation, South China University of Technology, Guangzhou 510640, PR China

[b]State Key Laboratory of Subtropical Building Science, South China University of Technology, Guangzhou 510640, PR China

[c]School of Engineering, University of Liverpool, Liverpool L69 3GH, UK

*Corresponding author: School of Civil Engineering and Transportation, South China University of Technology, Guangzhou 510640, PR China.

Abstract

The appearance of multiple cracks on engineering structures has a large influence on the structural dynamic characteristics. The Erdogan fundamental solutions for static analysis of an infinite single cracked plate are introduced in this paper. Using the multi-domain coupling technique, the multi-crack problem is transformed into several single crack problems. For each single crack problem, based on the above fundamental solutions, dynamic fracture analysis is presented with the mathematical formulation and computational implementation of the spline fictitious boundary element method (SFBEM). Here, the stress boundary conditions on the crack surface are automatically satisfied and the singular behaviour at the crack tip is naturally captured. The angular frequencies and mode shapes of the multi-crack problem are obtained using the proposed method. The dynamic stress intensity factors (DSIFs) of the multi-crack problem are also obtained. Numerical examples are given to demonstrate the accuracy of the proposed method in comparison to the finite element method.

Keywords: Dynamic analysis; Fracture mechanics; Spline fictitious boundary element method; Erdogan fundamental solutions

1 Introduction

Dynamic analysis including modal analysis and transient analysis is one of the major issues in structural analysis, since engineering structures often service under dynamic loadings [1,2]. Multiple cracks existing in structures have a large influence on the structural dynamic characteristics, which may lead to the final failure of the structures with cracks. Therefore, it is worthwhile to develop an effective numerical method to analyze the dynamic behavior of the structures with multiple cracks.

In the field of fracture mechanics, the finite element method (FEM), due to its considerably high efficiency, is the most commonly used approach for dynamic analysis of the crack problems [3–5]. However, in order to capture the crack singular behaviour, the finite element meshes need to be refined near the crack tip. For dynamic analysis of the multi-crack problem, the crack tips become more difficult to handle, so that the increase of degrees of freedom makes the solution very time-consuming. The extended finite element method (XFEM), as an improved FEM, introduces additional degrees of freedom to simulate the crack tips and has been applied to dealing with the dynamic crack problems [6–8]. However, dense meshes around crack tips are still necessary for obtaining accurate solutions, which causes high computational costs.

As an alternative method to FEM, the boundary element method (BEM) has been successfully applied to the dynamic crack problems. Compared with FEM, it only requires boundary discretizating rather than domain discretizating. The BEM has been successfully used to solve the dynamic crack problems in the Laplace domain [9,10], in the time domain based on the transient fundamental solutions [11,12] and in the time domain with the combination of the dual reciprocity techniques [13–15]. The first method increases the computational effort because of its complicated arithmetical operations. The second method needs analytical fundamental solutions within the time domain which are not given for every problem. To overcome these deficiencies, the dual reciprocity techniques are introduced into the BEM formulation so that the elastostatic fundamental solutions can be used for dynamic analysis. However, these BEM literatures mentioned above are all based on the non-crack fundamental solutions. Here, special elements, e.g. the isoparametric singular elements [16,17], need to be developed at the crack tips so as to capture the crack singular behaviour and also, the stress intensity factor (SIF) needs to be calculated using extra treatments (e.g. the extrapolation techniques and J-integral).

Different from the non-crack elasticity fundamental solutions, the Erdogan fundamental solutions [18,19] derived analytically from a single cracked infinite plane can be used directly in the BEM formulation for the crack problem [20]. Due to the use of these fundamental solutions, the singular behaviour at the crack tip can be naturally reflected and the stress boundary conditions along the crack surface can be automatically satisfied. What is more, SIFs can be calculated from the closed-form formulation using these fundamental solutions. In order to avoid the singular integral of the Erdogan fundamental solutions in terms of complex functions in the direct BEM, a non-singular BEM, i.e. the spline fictitious boundary element method (SFBEM) based on the Erdogan fundamental solutions, was proposed and used to solve the probabilistic single crack problem [21] and further extended to solve the static multi-crack problem [22] with the combination of the multi-domain coupling technique [23–25].

In this research, the multi-domain SFBEM based on the Erdogan fundamental solutions is extended to analyse the multi-crack dynamic problem. The Erdogan fundamental solutions for static analysis of an infinite cracked plate are first introduced in this paper. Then, with the help of the multi-domain coupling technique, the multi-cracked domain is divided into several single cracked domains. After that, the Erdogan fundamental solutions are adopted to present the mathematical formulation and computational implementation of SFBEM for modal analysis and transient analysis, respectively. Numerical results of the angular frequencies, the mode shapes and the dynamic stress intensity factors (DSIFs) of the multi-cracked plates are calculated to demonstrate the accuracy of the proposed method compared with the finite element method.

2 Erdogan fundamental solutions of plane crack problems

The Erdogan fundamental solutions for an infinite single cracked plane are introduced here. Then, the closed-form expressions of the strains for these fundamental solutions are further derived.

The fundamental solutions for a pair of concentrated forces in an infinite plane with a crack are used in this paper for the SFBEM formulations, which were formulated by Erdogan [18] for a linear, isotropic and homogeneous material. These solutions are presented below with the closed-form expressions of the displacements given in literature [22] recently.

Consider an infinite plane with a crack subjected to the concentrated forces Q and P at an arbitrary point $z_0=x_0+\mathrm{i}y_0$, as shown in Fig. 1. The stresses and displacements at an arbitrary point $z = x+i$ *("i" should not be Italic)* y and the stress intensity factors (SIFs) at crack tips can be expressed as

$$\left.\begin{aligned} \sigma_x+\sigma_y &= 2\left[\phi(z)+\overline{\phi(z)}\right] \\ \sigma_y-\sigma_x+2\mathrm{i}\tau_{xy} &= 2\left[(\bar{z}-z)\,\phi'(z)-\phi(z)+\overline{\boldsymbol{\Omega}(\bar{z})}\right] \end{aligned}\right\} \tag{1}$$

$$\begin{aligned} 2\mu(u+\mathrm{i}v) = {} & -\kappa S\ln\left[(z-z_0)(\bar{z}-\bar{z}_0)\right]+\frac{\bar{S}(\bar{z}_0-z_0)}{\bar{z}-\bar{z}_0} \\ & +(\bar{z}-z)\overline{\left(-\frac{S}{z-z_0}+\phi_0(z)\right)}+\kappa M(z,z_0)-M(\bar{z},z_0) \end{aligned} \tag{2}$$

$$\begin{aligned} K = {} & K_{\mathrm{I}}-\mathrm{i}K_{\mathrm{II}}=2\sqrt{2\pi}\lim_{z\to a}\left[\left(\sqrt{z-a}\right)\phi(z)\right] \\ = {} & \frac{1}{2\sqrt{\pi a}}\frac{1}{(1+\kappa)}\left\{(Q+\mathrm{i}P)\left[\left(\frac{a+z_0}{\sqrt{z_0^2-a^2}}-1\right)-\kappa\left(\frac{a+\bar{z}_0}{\sqrt{\bar{z}_0^2-a^2}}-1\right)\right]\right. \\ & \left.+\frac{a(Q-\mathrm{i}P)(\bar{z}_0-z_0)}{(\bar{z}_0-a)\sqrt{\bar{z}_0^2-a^2}}\right\} \end{aligned} \tag{3}$$

where

$$
\left.
\begin{aligned}
&\phi(z) = -\frac{S}{z-z_0} + \phi_0(z) \\
&\boldsymbol{\Omega}(z) = \frac{\kappa S}{z-\bar{z}_0} + \frac{\bar{S}(\bar{z}_0-z_0)}{(z-\bar{z}_0)^2} + \phi_0(z) \\
&\phi_0(z) = \frac{1}{2\pi\sqrt{z^2-a^2}}\left\{\frac{S}{z-z_0}\left[I(z)-I(z_0)\right] - \frac{\kappa S}{z-\bar{z}_0}\left[I(z)-I(\bar{z}_0)\right]\right. \\
&\qquad \left. -\bar{S}(\bar{z}_0-z_0)\left[\frac{I(z)-I(\bar{z}_0)}{(z-\bar{z}_0)^2} - \frac{J(\bar{z}_0)}{z-\bar{z}_0}\right]\right\} \\
&I(z) = \pi\left(\sqrt{z^2-a^2}-z\right) \\
&J(z) = \pi\left(\frac{z}{\sqrt{z^2-a^2}}-1\right) \\
&M(z,z_0) = \frac{S}{2}L(z,z_0) - -\frac{\kappa S}{2}L(z,\bar{z}_0) - \frac{\bar{S}(\bar{z}_0-z_0)}{2}\left[\frac{\sqrt{(z^2-a^2)}-\sqrt{\left(\bar{z}_0{}^2-a^2\right)}}{(z-\bar{z}_0)\sqrt{\left(\bar{z}_0{}^2-a^2\right)}}\right] \\
&L(z,z_0) = \ln\left[\frac{\sqrt{z^2-a^2}\sqrt{z_0^2-a^2}+z\cdot z_0-a^2}{\sqrt{z^2-a^2}+z)}\right] \\
&S = \frac{Q+\mathrm{i}P}{2\pi(1+\kappa)} \\
&\kappa = \begin{cases} 3-4\nu & \text{(Planestrain)} \\ \frac{3-\nu}{1+\nu} & \text{(Planestress)} \end{cases}
\end{aligned}
\right\}
\tag{4}
$$

("Planestrain" and "Planestress" should be "Plane strain" and "Plane stress", respectively.)

where $\overline{(\cdot)}$ means the conjugate complex number of (•).

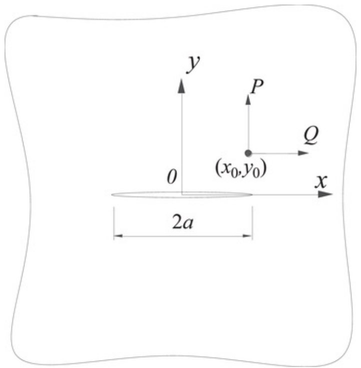

Fig. 1 Infinite plane with a crack.

alt-text: Fig 1

Moreover, with the consideration of the relationship between the stresses and the strains, the closed-form expressions of the strains for the Erdogan fundamental solutions are given as follows:

$$\left.\begin{aligned}\varepsilon_x+\varepsilon_y&=\frac{2(1-\nu)}{E}\left[\phi(z)+\overline{\phi(z)}\right]\ \text{(Plane stress)}\\ \varepsilon_x+\varepsilon_y&=\frac{2(1-2\nu)(1+\nu)}{E}\left[\phi(z)+\overline{\phi(z)}\right]\ \text{(Plane strain)}\\ \varepsilon_y-\varepsilon_x+\mathrm{i}\gamma_{xy}&=\frac{2(1+\nu)}{E}\left[(\bar{z}-z)\phi'(z)-\phi(z)+\overline{\boldsymbol{\Omega}(\bar{z})}\right]\end{aligned}\right\}\tag{5}$$

In the above equations, a is the half crack length. μ and ν are the shear modulus and the Poisson's ratio of the material, respectively. For the concentrated forces Q and P applied at an arbitrary point $z_0=x_0+iy_0$, σ_x, σ_y and τ_{xy} are the stresses at an arbitrary point $z=x+iy$ ("i" should not be Italic.); u and v are the displacements at an arbitrary point $z=x+iy$ ("i" should not be Italic.); ε_x, ε_y and ε_{xy} are the strains at an arbitrary point $z=x+iy$ ("i" should not be Italic.); K_{I} and K_{II} are SIFs at crack tips. Evidently, if we let $F=0$, $Q=1$ or $F=1$, $Q=0$ in Eqs. (1)~~to~~–(5), the Erdogan fundamental solutions become the fundamental solutions for plane crack problems.

A non-singular indirect boundary element method, SFBEM, based on the Erdogan fundamental solutions was applied to solving the probabilistic single crack problem [21] and the static multi-crack problem [22]. Because of the use of these fundamental solutions, the singularity at the crack tip can be naturally reflected and the stress boundary conditions along the crack surface can be automatically satisfied. In this research, the multi-domain SFBEM based on the Erdogan fundamental solutions is further extended to solve the dynamic multi-crack problem.

3 Modal analysis of multi-crack problems

3.1 Derivation of non-singular integral equations

Without loss of generality, consider an elastic double cracked plane domain Ω subjected to body forces, as shown in Fig. 2.

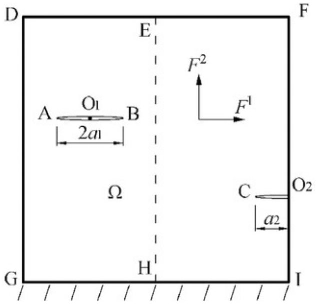

Fig. 2 The double cracked plane domain.

alt-text: Fig 2

The double cracked plane domain is divided into a single inner cracked subdomain and a single edge cracked subdomain, each of which is of uniform property and thickness. As shown in Fig. 3, point O_1 and point O_2 are the midpoints of crack AB and crack CJ, respectively. The common boundary of two subdomains is assumed to be Γ, and the boundary of the ith subdomain Ω_i is assumed to be L ("L" should not be Italic.)$_i$ ($i=1$, 2), without including the crack surface. Let the lengths of the inner crack and the edge crack be $2a_1$ and a_2, respectively. Assume the body forces to be the inertia forces F_i^l ($l=1$, 2) at an arbitrary points Q_{0i} within subdomain Ω_i, expressed as follows:

$$\left.\begin{aligned}F_i^1\left(Q_{0i},t\right)&=-\rho_i\left(Q_{0i}\right)\frac{\partial^2 u(Q_{0i},t)}{\partial t^2}\\ F_i^2\left(Q_{0i},t\right)&=-\rho_i\left(Q_{0i}\right)\frac{\partial^2 v(Q_{0i},t)}{\partial t^2}\end{aligned}\right\}\tag{6}$$

where $\rho_i(Q_{0i})$ is the volume density at an arbitrary point Q_{0i} within the ith subdomain Ω_i.

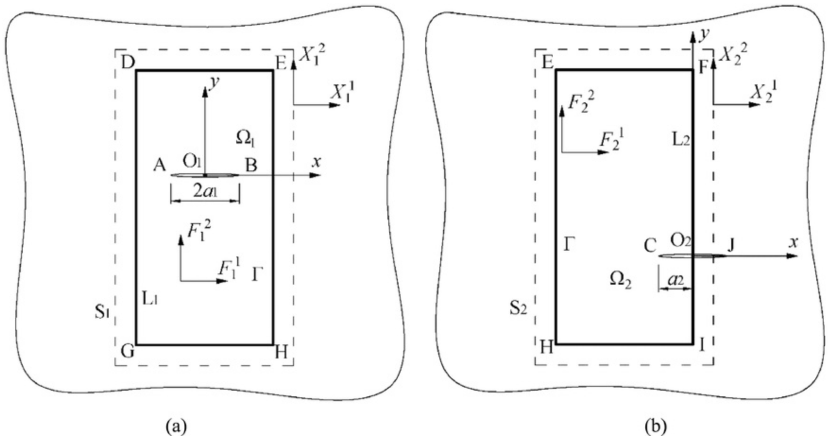

Fig. 3 Two subdomains embedded in an infinite domain—(a) the first subdomain with an inner crack, (b) the second subdomain with an edge crack.

alt-text: Fig 3

Firstly, each subdomain is embedded into an infinite single cracked plane with the crack length $2a_i$. Apply unknown fictitious loads X_i^l (l = 1, 2) along the fictitious boundary S_i outside Ω_i, whose shape is similar to that of the real boundary L_i ("L" should not be Italic.), as shown in Fig. 3. Then, under the combined action of the fictitious loads X_i^l and the inertia forces F_i^l and by using the Erdogan fundamental solutions, the components of displacements and stresses at an arbitrary point P_0 within the infinite domain corresponding to Ω_i are as follows:

$$\left.\begin{aligned}
u(P_0,t) &= \sum_{l=1}^{2}\int_{S_i} u^l(P_0;Q_i)X_i^l(Q_i,t)\,\mathrm{d}s + \sum_{l=1}^{2}\iint_{\Omega_i} u^l(P_0;Q_{0i})F_i^l(Q_{0i},t)\,\mathrm{d}\Omega \\
v(P_0,t) &= \sum_{l=1}^{2}\int_{S_i} v^l(P_0;Q_i)X_i^l(Q_i,t)\,\mathrm{d}s + \sum_{l=1}^{2}\iint_{\Omega_i} v^l(P_0;Q_{0i})F_i^l(Q_{0i},t)\,\mathrm{d}\Omega \\
\sigma_x(P_0,t) &= \sum_{l=1}^{2}\int_{S_i} \sigma_x^l(P_0;Q_i)X_i^l(Q_i,t)\,\mathrm{d}s + \sum_{l=1}^{2}\iint_{\Omega_i} \sigma_x^l(P_0;Q_{0i})F_i^l(Q_{0i},t)\,\mathrm{d}\Omega \\
\sigma_y(P_0,t) &= \sum_{l=1}^{2}\int_{S_i} \sigma_y^l(P_0;Q_i)X_i^l(Q_i,t)\,\mathrm{d}s + \sum_{l=1}^{2}\iint_{\Omega_i} \sigma_y^l(P_0;Q_{0i})F_i^l(Q_{0i},t)\,\mathrm{d}\Omega \\
\tau_{xy}(P_0,t) &= \sum_{l=1}^{2}\int_{S_i} \tau_{xy}^l(P_0;Q_i)X_i^l(Q_i,t)\,\mathrm{d}s + \sum_{l=1}^{2}\iint_{\Omega_i} \tau_{xy}^l(P_0;Q_{0i})F_i^l(Q_{0i},t)\,\mathrm{d}\Omega
\end{aligned}\right\} \tag{7}$$

where $Q_i \in S_i$, $Q_{0i} \in \Omega_i$; and u^l, v^l, σ^l_x, σ^l_y and τ^l_{xy} are the Erdogan fundamental solutions shown in Section 2.

Due to the use of the Erdogan fundamental solutions, not only the governing differential equations within Ω_i, but also the stress boundary conditions on the crack surface are satisfied automatically with Eq. (7). Therefore, only the boundary conditions and the continuity and equilibrium conditions along the contour of Ω_i need to be considered.

Substituting Eq. (7) into the boundary conditions [26] along L_i, one has

$$\begin{aligned}
&\sum_{l=1}^{2}\int_{S_i} G_{ik}^l(P_i;Q_i)X_i^l(Q_i,t)\,ds \\
&+ \sum_{l=1}^{2}\iint_{\Omega_i} G_{ik}^l(P_i;Q_{0i})F_i^l(Q_{0i},t)\,\mathrm{d}\Omega = 0 \quad \left(i = 1,2; k = 1,2 \right.
\end{aligned} \tag{8}$$

where $P_i \in L$ ("L" should not be Italic.)$_i$, and $k = 1, 2$ denotes the two boundary conditions along boundary L_i ("L" should not be Italic.) for plane problems; and $G_{ik}^{\,l}$ are the kernel functions consisting of the Erdogan fundamental solutions.

In addition to the boundary conditions along L_i ("L" should not be Italic.), the displacement continuity conditions and stress equilibrium conditions along the common boundary Γ should also be satisfied. Substituting Eq. (7) into the continuity and equilibrium conditions [26] along the common boundary Γ, one has

$$\begin{aligned} &\sum_{l=1}^{2}\int_{S_1} G_{1k}^{l}\left(P;Q_1\right) X_1^l\left(Q_1,t\right)\mathrm{d}s + \sum_{l=1}^{2}\iint_{\Omega_1} G_{1k}^{l}\left(P;Q_{01}\right) F_i^l\left(Q_{01},t\right)\mathrm{d}\Omega \\ &= \sum_{l=1}^{2}\int_{S_2} G_{2k}^{l}\left(P;Q_2\right) X_2^l\left(Q_2,t\right)\mathrm{d}s + \sum_{l=1}^{2}\iint_{\Omega_2} G_{2k}^{l}\left(P;Q_{02}\right) F_i^l\left(Q_{02},t\right)\mathrm{d}\Omega \\ &\qquad (k = 1,2,3,4) \end{aligned} \tag{9}$$

where $P \in \Gamma$, ("L" should not be Italic.) $k = 1,2,3,4$ donates the two displacement continuity conditions and two stress equilibrium conditions along Γ ("Γ" should not be Italic.); and $G_{ik}^{\,l}$ are the kernel functions consisting of the Erdogan fundamental solutions.

3.2 Numerical methods

As the source points will never coincide with the field points in the kernel functions, Eqs. (8) and (9) are both non-singular fictitious boundary integral equations. Generally, analytical solutions for Eqs. (8) and (9) cannot be obtained directly, and a numerical measure must be used to solve the integral equations.

The fictitious boundary S_i is divided into N_i divisions and N_i +1 nodes are obtained, and the element between two adjacent spline nodes is termed as a fictitious boundary element. Then the unknown fictitious $X_i^l(s, t)$ are expressed in terms of a set of B-spline functions as follows [23]:

$$X_i^l(s,t)\ \sum_{n=-1}^{N_i+1} x_{in}^l(t)\,\varphi_n(s) \quad (l = 1,\, 2) \tag{10}$$

where s is the local coordinate along S_i; x^l_{in} are the unknown spline node parameters; and $\phi_n(s)$ are B-spline functions of the third order [27].

Annotations:

A1. "="should be added between two expressions.

The boundary L_i and the common boundary Γ are divided into a sufficient number of segments. At the same time, the subdomain Ω_i is divided into N_i cells and the inertia forces F_i^l are assumed to concentrate at the central points of the n-th cell ($n = 1,2, \ldots, N_i$) within the ith subdomain, which can be written as

$$\left.\begin{aligned} F_i^1\left(Q_{ni},t\right) &= -\Delta A_{ni}\rho_i\left(Q_{ni}\right)\frac{\partial^2 u(Q_{ni},t)}{\partial t^2} \\ F_i^2\left(Q_{ni},t\right) &= -\Delta A_{ni}\rho_i\left(Q_{ni}\right)\frac{\partial^2 v(Q_{ni},t)}{\partial t^2} \end{aligned}\right\} \tag{11}$$

where ΔA_{ni} is the area of the n-th cell within the ith subdomain; and Q_{ni} is the coordinate of the central point of the n-th cell within the ith subdomain.

Substituting Eqs. (10) and (11) into Eqs. (8) and (9) and let the integrations of the residues along each segment along the boundary L_i and the common boundary Γ be zero, one can obtain

$$\left[G_i\right]\left\{X_i(t)\right\} + \left[B_i\right]\left(-\left[M_i\right]\left\{\ddot{D}_i(t)\right\}\right) = \{0\} \tag{12}$$

$$\left[g_1\right]\left\{X_1(t)\right\} + \left[b_1\right]\left(-\left[M_1\right]\left\{\ddot{D}_1(t)\right\}\right) = \left[g_2\right]\left\{X_2(t)\right\} + \left[b_2\right]\left(-\left[M_2\right]\left\{\ddot{D}_2(t)\right\}\right) \tag{13}$$

where $\{X_i(t)\}$ denotes the column matrix consisting of the unknown spline node parameters of the fictitious loads along S_i; $[G_i]$ and $[g_i]$ denote the influence matrices of $\{X_i(t)\}$ corresponding to the boundary conditions and the common conditions, respectively; $[B_i]$ and $[b_i]$ denote the influence matrices of the inertia forces corresponding to the boundary conditions and the common boundary conditions, respectively; and $[M_i]$ denotes the mass matrix and $\left\{\ddot{D}_i(t)\right\}$ denotes the column matrix of acceleration components within Ω_i.

Eqs. (12) and (13) can be combined into one overall equation as follows:

$$[G]\{X(t)\} + [B]\left(-[M]\left\{\ddot{D}(t)\right\}\right) = \{0\} \tag{14}$$

where the overall matrices in the equation are dependent on the corresponding matrices in Eqs. (12) and (13).

To further establish ~~the~~ Eq. (14), the supplementary equation is required. Discretizing the fictitious loads and the inertia forces from the first two equations of Eq. (7) with the same treatment, the displacement column matrix $\{D(t)\}$ of two subdomains can be obtained as

$$\{D(t)\} = \left[\widetilde{G}\right]\{X(t)\} + \left[\widetilde{B}\right]\left(-[M]\left\{\ddot{D}(t)\right\}\right) \tag{15}$$

where $\left[\widetilde{G}\right]$ and $\left[\widetilde{B}\right]$ denote the influence matrices of $\{X(t)\}$ and the inertia forces according to the displacement column matrix $\{D(t)\}$, respectively.

With the consideration of Eqs. (14) and (15), $\{X(t)\}$ can be solved as

$$\{X(t)\} = [G]^{-1}[B][M]\left\{\ddot{D}(t)\right\} \tag{16}$$

Substituting Eq. (16) into Eq. (15), one has

$$[\delta][M]\left\{\ddot{D}(t)\right\} + \{D(t)\} = \{0\} \tag{17}$$

where

$$[\delta] = \left[\widetilde{B}\right] - \left[\widetilde{G}\right][G]^{-1}[B] \tag{18}$$

Eq. (17) is the equation for modal analysis of the elastic plane crack problems, and $[\delta]$ is the flexibility matrix.

3.3 Analysis of the angular frequencies and displacement modes

Eq. (18) is the homogeneous linear equation with constant coefficients and thus, the solutions can be expressed as

$$\{D(t)\} = \left\{D_0\right\} sin\omega t \tag{19}$$

A1

where ω denotes the angular frequency and $\{D_0\}$ denotes the column matrix of the displacement mode related to ω.

Annotations:

A1. "sin" should not be Italic.

Substituting Eq. (19) into Eq. (17), there is

$$\left(-\omega^2[\delta][M] + [I]\right)\left\{D_0\right\} = \{0\} \tag{20}$$

where $[I]$ is the unit matrix. Eq. (20) can be converted into a standard eigenvalue problem as follows:

$$\lambda\left\{D_0\right\} = [\delta][M]\left\{D_0\right\} \tag{21}$$

where $\lambda = 1/\omega^2$. The eigenvalue λ and the corresponding displacement mode column matrix $\{D_0\}$ can be obtained by solving Eq. (21).

The angular frequency can be obtained as follows:

$$\omega = \sqrt{\frac{1}{\lambda}} \tag{22}$$

It should be noted that, in the above formulations for modal analysis of crack plane structures, the contact condition of crack surfaces is not taken into consideration. Actually, the mode shapes and the corresponding frequencies obtained from modal analysis of a cracked structure are used to solve the transient dynamic problem with the mode superposition method, in which the cracked structure is assumed to be subjected to dynamic tensions without contact of the crack surfaces. This means that, in the process of transient vibration, the cracked structure will behave linearly with a constant stiffness matrix. Therefore, modal analysis of cracked structures are generally conducted without consideration of the contact of crack surfaces, which can be shown in Ref~~erence~~s. [28~~] and [~~,29].

3.4 Analysis of the strain modes

Similar to Eq. (7), under the combined action of the fictitious loads X_i^l and the inertia forces F_i^l ($l = 1, 2$), the components of the strains at an arbitrary point P_0 in the infinite domain corresponding to Ω_i are as follows:

$$\left.\begin{aligned}
\varepsilon_x\left(P_0, t\right) &= \sum_{l=1}^{2}\int_{S_i}\varepsilon_x^l\left(P_0; Q_i\right) X_i^l\left(Q_i, t\right)\mathrm{d}s + \sum_{l=1}^{2}\iint_{\Omega_i}\varepsilon_x^l\left(P_0; Q_{0i}\right) F_i^l\left(Q_{0i}, t\right)\mathrm{d}\Omega \\
\varepsilon_y\left(P_0, t\right) &= \sum_{l=1}^{2}\int_{S_i}\varepsilon_y^l\left(P_0; Q_i\right) X_i^l\left(Q_i, t\right)\mathrm{d}s + \sum_{l=1}^{2}\iint_{\Omega_i}\varepsilon_y^l\left(P_0; Q_{0i}\right) F_i^l\left(Q_{0i}, t\right)\mathrm{d}\Omega \\
\gamma_{xy}\left(P_0, t\right) &= \sum_{l=1}^{2}\int_{S_i}\gamma_{xy}^l\left(P_0; Q_i\right) X_i^l\left(Q_i, t\right)\mathrm{d}s + \sum_{l=1}^{2}\iint_{\Omega_i}\gamma_{xy}^l\left(P_0; Q_{0i}\right) F_i^l\left(Q_{0i}, t\right)\mathrm{d}\Omega
\end{aligned}\right\}\tag{23}$$

where ε_x^l, ε_y^l and γ_{xy}^l are the closed-form expressions of the strains given in the Erdogan fundamental solutions shown in Section 2.

After the discretization of the strains, the fictitious loads and the inertia forces, the strain column matrix $\{\varepsilon_i(t)\}$ of the ith subdomain can be obtained by Eq. (23) as follows:

$$\left\{\varepsilon_i(t)\right\} = \left[\widetilde{G}_{\varepsilon i}\right]\left\{X_i(t)\right\} + \left[\widetilde{B}_{\varepsilon i}\right]\left(-\left[M_i\right]\left\{\ddot{D}_i(t)\right\}\right)\tag{24}$$

where $\left[\widetilde{G}_{\varepsilon i}\right]$ and $\left[\widetilde{B}_{\varepsilon i}\right]$ denote the influence matrices of $\{X_i(t)\}$ and the inertia forces $-\left[M_i\right]\left\{\ddot{D}_i(t)\right\}$ corresponding to the strain column matrix $\{\varepsilon_i(t)\}$, respectively.

With the consideration of the strains for all the subdomains, Eq. (24) can be written as

$$\{\varepsilon(t)\} = \left[\widetilde{G}_{\varepsilon}\right]\{X(t)\} + \left[\widetilde{B}_{\varepsilon}\right]\left(-[M]\left\{\ddot{D}(t)\right\}\right)\tag{25}$$

Substituting Eq. (16) into Eq. (25), one has

$$\{\varepsilon(t)\} = \left[\delta_{\varepsilon}\right]\left(-[M]\left\{\ddot{D}(t)\right\}\right)\tag{26}$$

where

$$\left[\delta_{\varepsilon}\right] = \left[\widetilde{B}_{\varepsilon}\right] - \left[\widetilde{G}_{\varepsilon}\right][G]^{-1}[B]\tag{27}$$

$\{\varepsilon(t)\}$ can be expressed as

$$\{\varepsilon(t)\} = \left\{\varepsilon_0\right\}\sin\omega t\tag{28}$$

where ω denotes the angular frequency and $\{\varepsilon_0\}$ denotes the column matrix of the strain mode corresponding to ω.

Substituting Eqs. (28) and (19) into Eq. (26), one has

$$\left\{\varepsilon_0\right\} = \omega^2\left[\delta_{\varepsilon}\right][M]\left\{D_0\right\}\tag{29}$$

It can be seen that once the displacement mode column matrix $\{D_0\}$ is obtained, the strain mode column matrix $\{\varepsilon_0\}$ can be obtained by using Eq. (29).

4 Transient analysis of multi-crack problems

For transient analysis of multi-crack problems, the elastic cracked plane domain Ω is generally not only affected by the inertial forces, but also by the damping loads and the external body loads. Therefore, Eq. (6) is modified as

$$\left.\begin{aligned}
F_i^1\left(Q_{0i}, t\right) &= -\rho_i\left(Q_{0i}\right)\frac{\partial^2 u(Q_{0i}, t)}{\partial t^2} - c_i\left(Q_{0i}\right)\frac{\partial u(Q_{0i}, t)}{\partial t} + f_i^1\left(Q_{0i}, t\right) \\
F_i^2\left(Q_{0i}, t\right) &= -\rho_i\left(Q_{0i}\right)\frac{\partial^2 v(Q_{0i}, t)}{\partial t^2} - c_i\left(Q_{0i}\right)\frac{\partial v(Q_{0i}, t)}{\partial t} + f_i^2\left(Q_{0i}, t\right)
\end{aligned}\right\}\tag{30}$$

where $c_i(Q_{0i})$ is the damping coefficient within the ith subdomain; and $f_i^l\left(Q_{0i}, t\right)$ $(l = 1, 2)$ are external body loads in either x or y direction within the ith subdomain.

Considering the boundary conditions, as shown in Fig. 4, not be zero, the non-singular integral Eq. (8) is modified as

$$\sum_{l=1}^{2}\int_{S_i} G_{ik}^{l}\left(P_i;Q_i\right) X_i^{l}\left(Q_i,t\right)\mathrm{d}s+\sum_{l=1}^{2}\int\int_{\Omega_i} G_{ik}^{l}\left(P_i;Q_{0i}\right) F_i^{l}\left(Q_{0i},t\right)\mathrm{d}\Omega=H_{ik}\left(P_i,t\right) \tag{31}$$

where H_{ik} denote the known boundary functions along Li.

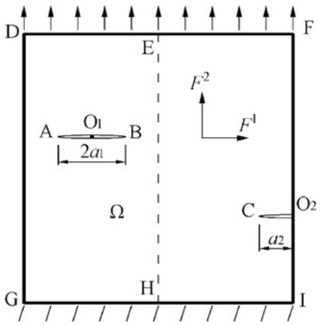

Fig. 4 The double cracked plane domain with non zero boundary conditions.

alt-text: Fig 4

After these modifications, Eq. (9) for the common boundary conditions can still be used in transient analysis. The subdomain Ω_i is divided into N_i cells, and the body forces $F_i^1\left(Q_{0i},t\right)$ $F_i^l\left(Q_{0i},t\right)$ in Eq. (30) are assumed to concentrate at the central points of the n-th cell (n = 1,2, ..., N_i). The concentrated forces can be expressed as

$$\left.\begin{aligned} F_i^1\left(Q_{ni},t\right)&=\Delta A_{ni}\left(-\rho_i\left(Q_{ni}\right)\frac{\partial^2 u(Q_{ni},t)}{\partial t^2}-c_i\left(Q_{ni}\right)\frac{\partial u(Q_{ni},t)}{\partial t}+f_i^1\left(Q_{ni},t\right)\right)\\ F_i^2\left(Q_{ni},t\right)&=\Delta A_{ni}\left(-\rho_i\left(Q_{ni}\right)\frac{\partial^2 v(Q_{ni},t)}{\partial t^2}-c_i\left(Q_{ni}\right)\frac{\partial v(Q_{ni},t)}{\partial t}+f_i^2\left(Q_{ni},t\right)\right)\end{aligned}\right\} \tag{32}$$

where ΔA_{ni} is the area of the n-th cell in the ith subdomain; and Q_{ni} is the coordinate of the central point of the n-th cell within the ith subdomain.

With the same treatments as those used in modal analysis, the algebraic equation can be obtained as

$$[G]\{X(t)\}+[B]\left(-[M]\left\{\ddot{D}(t)\right\}-[C]\left\{\dot{D}(t)\right\}+\{f(t)\}\right)=\{H(t)\} \tag{33}$$

where $\{X(t)\}$, $[G]$, $[M]$ and $\left\{\ddot{D}(t)\right\}$ are the same with the corresponding matrices in Eq. (14); $\{f(t)\}$ denotes the column matrix discretized by the external loads; $[C]$ denotes the damping matrix determined using the Rayleigh damping assumption; $\left\{\dot{D}(t)\right\}$ denotes the column matrix of velocity components; and $\{H(t)\}$ denotes the known column matrix depending on the boundary conditions.

In addition, the supplementary Eq. (15) should be modified as

$$\{D(t)\}=\left[\widetilde{G}\right]\{X(t)\}+\left[\widetilde{B}\right]\left(-[M]\left\{\ddot{D}(t)\right\}-[C]\left\{\dot{D}(t)\right\}+\{f(t)\}\right) \tag{34}$$

Eliminating $\{X(t)\}$ from Eqs. (33) and (34), one has

$$[\delta][M]\left\{\ddot{D}(t)\right\}+[\delta][C]\left\{\dot{D}(t)\right\}+\{D(t)\}=\left[\widetilde{G}\right][G]^{-1}\{H(t)\}+[\delta]\{f(t)\} \tag{35}$$

Eq. (35) is the equation of motion and can be solved by using either the mode superposition method or the Newmark-β method [30] to obtain $\left\{\ddot{D}(t)\right\}$, $\left\{\dot{D}(t)\right\}$ and $\{D(t)\}$. Then, $\{X(t)\}$ can be calculated with the consideration of Eq. (33) as follows:

$$\{X(t)\}=[G]^{-1}\left(\{H(t)\}+\left([B][M]\left\{\ddot{D}(t)\right\}+[C]\left\{\dot{D}(t)\right\}-\{f(t)\}\right)\right) \tag{36}$$

Once the spline node parameter $\{X(t)\}$ is determined, the mode-I and mode-II SIFs of the jth crack within the ith subdomain can be calculated using the following equation:

$$K_{ij}(t) = \sum_{l=1}^{2} \int_{S} K_{ij}^{l}(P_0; Q_i)\, X_i^{l}(Q_i, t)\, \mathrm{d}s + \sum_{l=1}^{2} \iint_{\Omega} K_{ij}^{l}(P_0; Q_{0i})\, F_i^{l}(Q_{0i}, t)\, \mathrm{d}\Omega \tag{37}$$

where $K_{ij}^{l}\,(i = 1, 2; j = \mathrm{I}, \mathrm{II}; l = 1, 2)$ are the fundamental solutions of SIFs corresponding to Ω_i.

5 Numerical examples

Numerical examples for three linear-elastic plane stress multi-crack problems are presented in this section. For all three examples, the modulus of elasticity and the Poisson's ratio of the material are assumed to be $E = 200$ GPa and $\nu = 0.3$, respectively. The mass density and the plate thickness are taken to be $\rho = 7800\,\mathrm{kg/m^3}$ and $t = 1$ mm, respectively. The time step is set to be $\Delta t = 0.3$ μs in the Newmark-β integral scheme. The weighting factors γ and β in the Newmark-β method are assumed to be $\gamma = 0.5$ and $\beta = 0.25$, respectively. The Rayleigh damping model is used for the plate with the damping ratio being taken to be $\zeta = 0.05$.

5.1 A square plate with two inner cracks

A double inner cracked square plate, as shown in Fig. 5, is analyzed. Point O_1 and point O_2 are the midpoints of the left and right cracks, respectively. As shown in Fig. 5, two cracks with four crack tips, namely A, B, C and D, are distributed in the plate, and the lengths of the left crack and the right crack are $2a_1$ and $2a_2$, respectively.

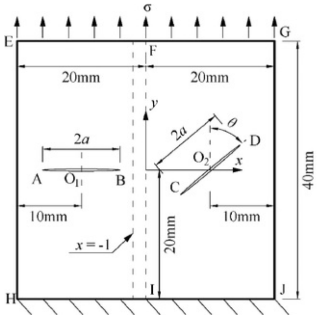

Fig. 5 A square plate with two inner cracks. (Figures and Tables in the numerical examples should be placed following the related numercial examples. However, in the PageProof, those Figures and Tables are too far from the related numerical examples. Please adjust the positions of Figures and Tables in th PageProof.)

alt-text: Fig 5

SFBEM based on the Erdogan fundamental solutions is used to calculate the DSIF values of four crack tips. As shown in Fig. 6, the plate is divided into two single inner cracked subdomains. In each subdomain, the number of the fictitious boundary element is taken to be N_s and the number of boundary segments is taken to be $2N_s$. The distance between the real boundary and the fictitious boundary in each subdomain is taken as the length of the boundary segment [23]. The plate is discretized into N_c cells, with the inertia loads concentrating at the center of each cell.

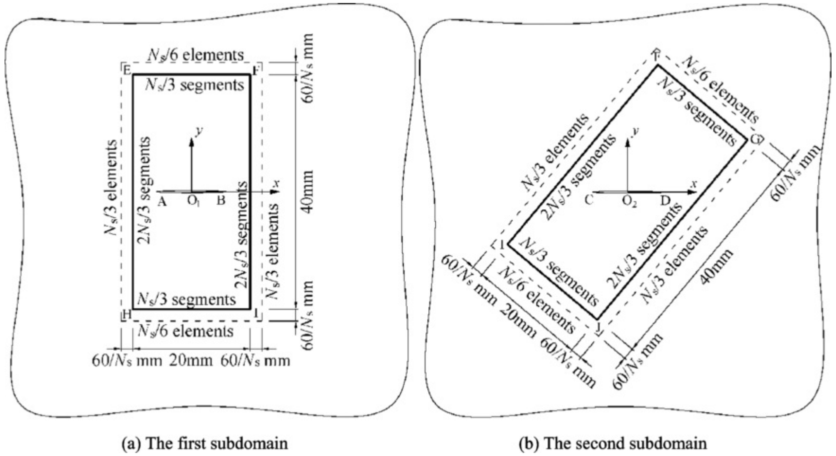

Fig. 6 Computational models for the two inner cracked subdomains.

alt-text: Fig 6

A convergence study for SFBEM is performed. Let the lengths of two cracks and the angle of the right crack be $2a_1 = 2a_2 = 10$ mm and $\theta = 45°$, respectively. For all numerical integrations along the boundary, 5 Gauss points are used. Firstly, for the convergence study for the number of fictitious boundary elements, the number of cells within the domain is fixed as 380, and the numbers of fictitious boundary elements in each subdomain are taken to be 18, 30, 60 and 120, respectively. Then, for the convergence study of number of cells within the domain, the number of fictitious boundary elements is fixed as 30, and the numbers of cells are taken to be 110, 203 and 380, respectively. The results from ~~the finite element method (~~FEM~~)~~ with 2021 elements which are fine enough are used as the reference solutions. The angular frequencies of the first six orders with different numbers of fictitious boundary elements and these with different numbers of cells are shown in Tables 1 and 2, respectively.

Table 1 The frequencies of the first six orders with different numbers of fictitious boundary elements (rad/s).

alt-text: Table 1

Order	FEM	SFBEM							
		$N_s = 18$	Relative Error	$N_s = 30$	Relative Error	$N_s = 60$	Relative Error	$N_s = 120$	Relative Error
1	78972.0	79310.5	0.43%	79056.5	0.11%	78848.3	0.16%	78809.3	0.21%
2	182846.0	179022.4	2.09%	183715.5	0.48%	183658.7	0.44%	183643.9	0.44%
3	216480.0	214854.2	0.75%	217147.8	0.31%	217148.1	0.31%	217121.7	0.30%
4	348817.0	343362.5	1.56%	349637.0	0.24%	349682.9	0.25%	349631.5	0.23%
5	353931.0	351960.5	0.56%	354796.7	0.24%	354261.6	0.09%	353964.3	0.01%
6	399838.0	394743.5	1.27%	397297.1	0.64%	396869.5	0.74%	396717.5	0.78%

Table 2 The frequencies of the first six orders of with different numbers of cells (rad/s).

alt-text: Table 2

Order	FEM	SFBEM					
		$N_c = 110$	RelativeError	$N_c = 203$	RelativeError	$N_c = 380$	RelativeError
1	78972.0	79054.6	0.10%	79090.7	0.15%	79056.5	0.11%

2	182846.0	182364.4	0.26%	183626.3	0.43%	183715.5	0.48%
3	216480.0	215540.9	0.43%	216907.3	0.20%	217147.8	0.31%
4	348817.0	343071.9	1.65%	347851.4	0.28%	349637.0	0.24%
5	353931.0	345256.2	2.45%	352396.7	0.43%	354796.7	0.24%
6	399838.0	384528.1	3.83%	393095.9	1.69%	397297.1	0.64%

Table 1 shows that the results of SFBEM agree well with those of FEM, which indicates that high accuracy can be achieved with fewer numbers of the fictitious boundary elements. When the number of fictitious boundary elements is larger than 30, the errors of all the six orders' frequencies predicted by SFBEM in comparison to those obtained from FEM are lower than 1%. Table 2 shows that the relative errors of high-order frequencies decrease obviously as the number of cells increases, indicating that the accuracy of frequencies increases with the increase of the number of cells.

Then, modal analysis for the plate is further studied. Let the lengths of two cracks and the angle of the right crack be $2a_1 = 2a_2 = 4\,\mathrm{mm}$ and $\theta = 30°$, respectively. For each subdomain, 30 fictitious boundary elements and 360 cells are used in SFBEM. The results calculated by FEM with 2122 finite elements are also shown as the reference solutions. The angular frequencies of the first six orders are listed in Table 3. The horizontal displacement results u_x of the 1st, 3rd and 5th orders of partial points on $x = -1$ are shown in Fig. 7. The strain mode of the first order are shown in Fig. 8.

Table 3 Frequencies of the first six orders (rad/s).

alt-text: Table 3

Order	FEM	SFBEM	Relative Error
1	82715.0	82727.8	0.02%
2	197843.0	197325.1	0.26%
3	223330.0	222811.0	0.23%
4	355424.0	353665.3	0.49%
5	380555.0	376718.2	1.01%
6	405122.0	401230.6	0.96%

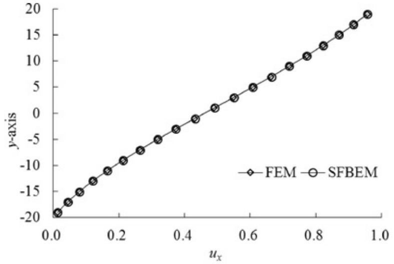

(a) The 1st order

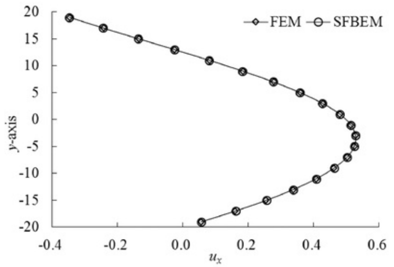

(b) The 3rd order

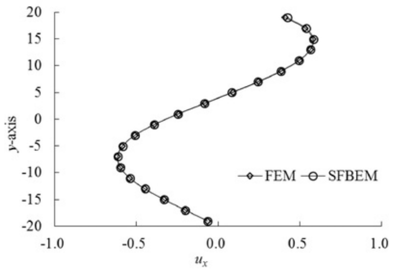

(c) The 5th order

Fig. 7 The horizontal displacement modes u_x of the first five orders of partial points on $x = -1$.

alt-text: Fig 7

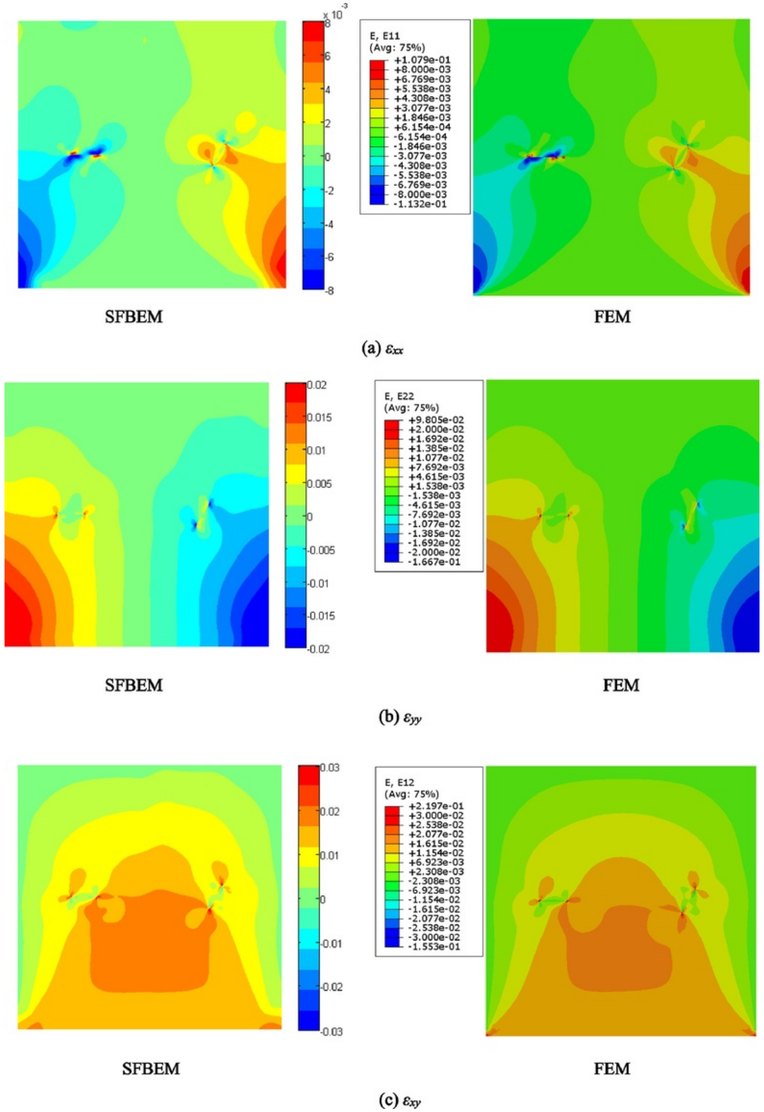

Fig. 8 The strain modes of the first order.

alt-text: Fig 8

It can be seen from Table 3, Figs. 7 and 8 that the results of SFBEM agree well with those of FEM, which indicates high accuracy of the present method. The results in Fig. 8 show that the appearance of cracks greatly affects the distribution of strain modes, as significant strain concentrations occur near the crack tips.

Finally, transient analysis for the plate is studied. A suddenly imposed uniform tensile load $\sigma(t)$ is shown in Fig. 9. The length of the left crack is fixed as $2a_1 = 10$ mm. DSIF values with different length $2a_2$ and angle θ of crack tip D are calculated. When consider varying the length $2a_2$, the angle θ of the right crack is fixed as 45°, while length $2a_2$ of the right crack are 4, 6, 8 and 10 mm, respectively. When consider varying the angle θ, the length $2a_2$ of the right crack is fixed as 10 mm, while the angle θ of the right crack is 30°, 45° and 60°, respectively. In SFBEM, for all cases, 30 fictitious boundary elements and 60 boundary segments are adopted in each subdomain, and the distance between the fictitious boundary and the real boundary in each subdomain is taken to be 2 mm. The number of cells in SFBEM and the number of finite elements in FEM under different cases are listed in Tables 4 and 5, respectively.

DSIFs K_I and K_{II} of crack tip D obtained with different crack lengths by SFBEM and FEM are presented in Figs. 10 and 11, while those obtained with different crack angles by SFBEM and FEM are presented in Figs. 12 and 13.

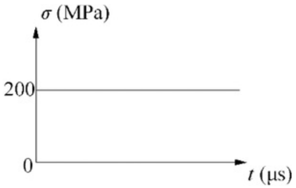

Fig. 9 The load function.

alt-text: Fig 9

Table 4 The number of cells in SFBEM under different cases.

alt-text: Table 4

Method	Number of cells					
	θ=45°			2a=10mm		
	2a_2=4 mm	2a_2=6 mm	2a_2=8 mm	θ=30°	θ=45°	θ=60°
SFBEM	380	380	380	360	380	400

Table 5 The number of finite elements in FEM under different cases.

alt-text: Table 5

Method	Number of finite elements					
	θ=45°			2a=10mm		
	2a_2=4 mm	2a_2=6 mm	2a_2=8 mm	θ=30°	θ=45°	θ=60°
FEM	2145	2100	2210	2020	2021	2071

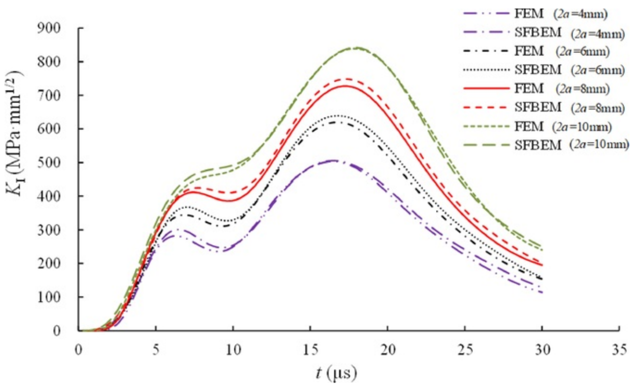

Fig. 10 (Shrink the figure so as to fit one column in the PageProof.) K_I of crack tip D obtained with different crack lengths.

alt-text: Fig 10

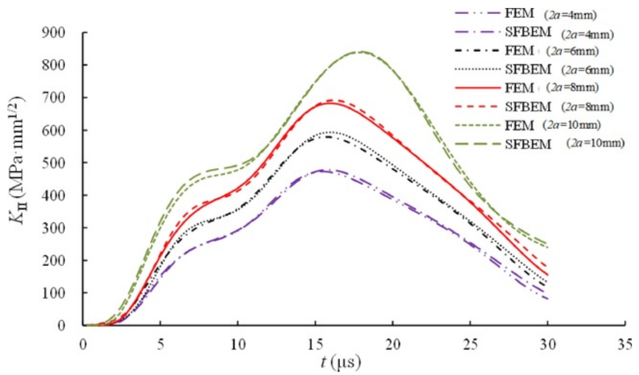

Fig. 11 **(Shrink the figure so as to fit one column in the PageProof.)** K_{II} of crack tip D obtained with different crack lengths.

alt-text: Fig 11

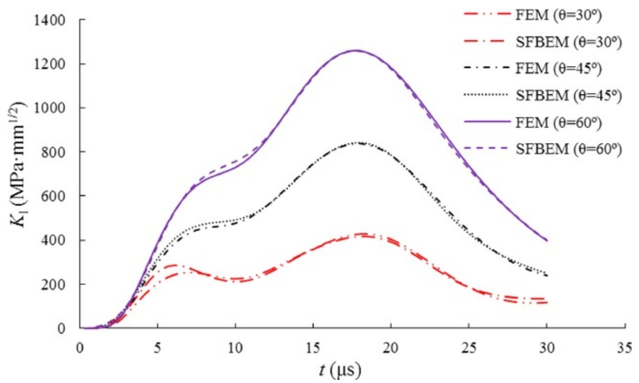

Fig. 12 (Shrink the figure so as to fit one column in the PageProof.) K_I of crack tip D obtained with different crack angles.

alt-text: Fig 12

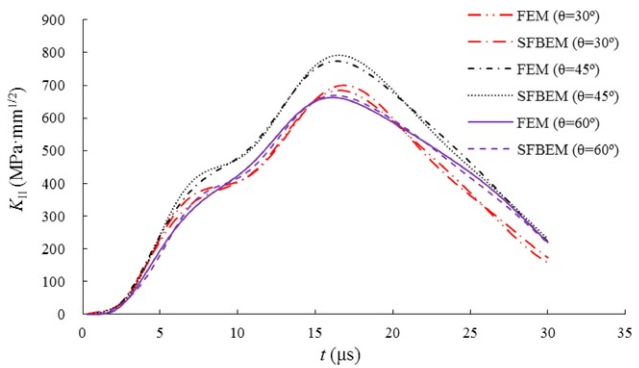

Fig. 13 **(Shrink the figure so as to fit one column in the PageProof.)** K_{II} of crack tip D obtained with different crack angles.

alt-text: Fig 13

It can be seen from Figs. 10 to 13 that DSIF results of SFBEM agree well with those of FEM, which again indicates high accuracy of the present method. Figs. 10 and 11 show that the shapes of curves under different crack lengths are similar, but the peak values of K_{I} and K_{II} increase with the increase of the crack length. It indicates that the longer the crack length is, the more likely the plate is damaged, which is consistent with the actual situation. Fig. 12 shows that the slope of curves increases with the increase of the crack angles. However, from Fig. 13, it can be seen that the values of K_{II} reach the maximum when the crack angle is 45°.

5.2 A rectangular plate with two edge cracks

A double edge cracked rectangular plate, as shown in Fig. 14, is analyzed. A suddenly imposed uniform tensile load $\sigma(t)$=[20sin(60000πt) + 200] MPa, as shown in Fig. 15, is applied at the top surface of the plate. The size of plate is 20 mm × 60 mm. The lengths of two horizontal edge cracks are taken to be 'a'. The crack length a varies from 1 mm to 3 mm.

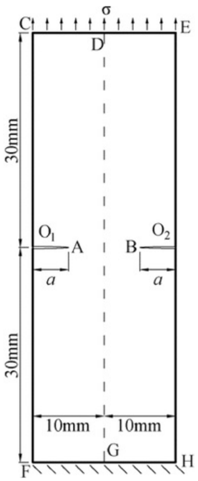

Fig. 14 A rectangular plate with two edge cracks.

alt-text: Fig 14

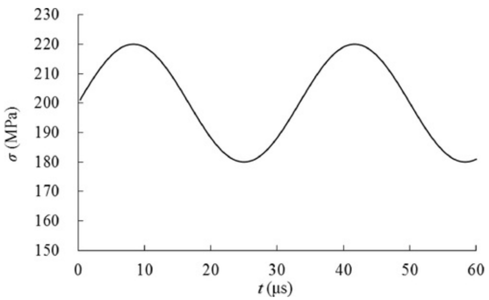

Fig. 15 The load function.

alt-text: Fig 15

The strain modes and DSIFs are calculated by SFBEM with the computational models in Fig. 16. It should be noted that since the stress distribution at the boundary near the edge crack is complicated, more fictitious boundary elements and boundary segments are needed. The plate is divided into two single edge cracked subdomains, in each of which 226 fictitious boundary elements and 452 boundary segments are adopted, and the distance between the fictitious boundary and the real boundary is taken to be 1 mm. 5 Gauss points are used. 200 cells are used for all SFBEM computations. The well-established finite element analysis is used for the comparison. The rectangular plate is divided into 1528, 1504 and 1406 elements for 1 mm, 2 mm and 3 mm of 'a', respectively. The frequencies of the first six orders with different crack lengths are shown in Fig. 17. The strain mode shapes ε_{yy} of the first order with different crack lengths are shown in Fig. 18. K_{I} of the crack tip A with different crack lengths are shown in Fig. 19.

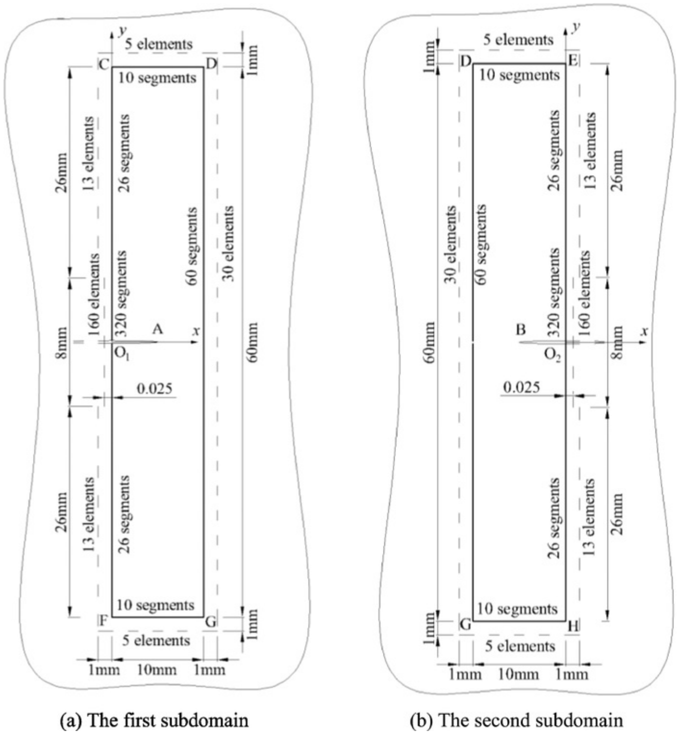

Fig. 16 Computational models for the two edge cracked subdomains.

alt-text: Fig 16

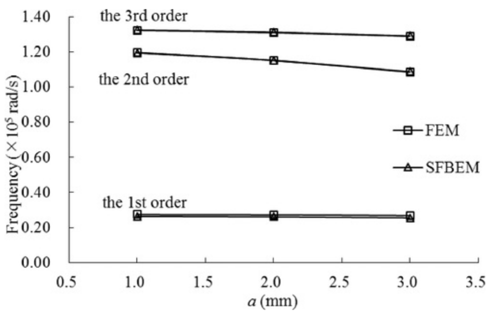

Fig. 17 The frequencies of the first three orders with different crack lengths.

alt-text: Fig 17

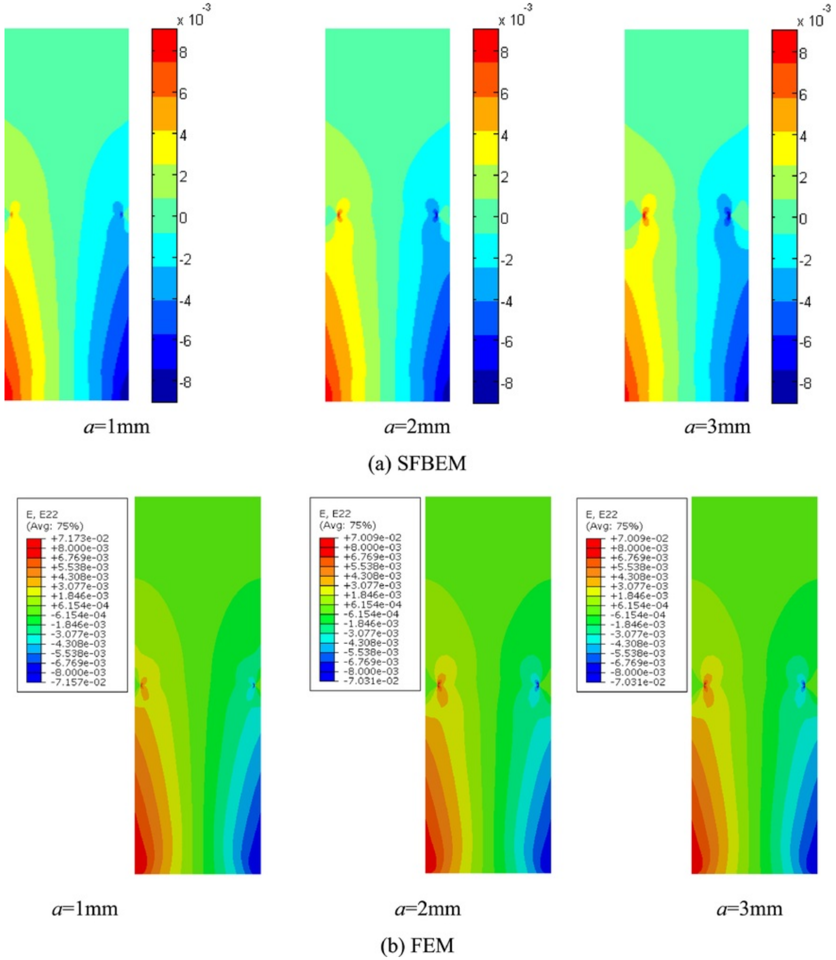

Fig. 18 The strain mode shapes ε_{yy} of the first order.

alt-text: Fig 18

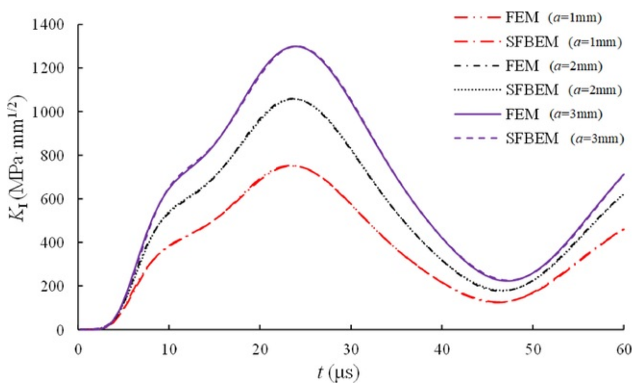

Fig. 19 (Shrink the figure so as to fit one colunm in the PageProof.) K_{I} of crack tip A obtained with different crack lengths.

alt-text: Fig 19

It can be seen from Fig. 17 that the frequencies of first three orders obtained by SFBEM agree well with those by FEM. As the crack length increases, the 1st order frequency decreases slightly, while those of 2nd and 3rd orders decrease more greatly.

From Fig. 18, we can see that the strain mode ε_{yy} related to the first order frequency calculated using SFBEM are also in a good agreement with those from FEM. The strain concentrations can be observed at the crack tips and the position of these concentrations changes as the crack length increases.

It can be seen from Fig. 19 that the tendency of DSIFs for different crack lengths calculated by SFBEM are the same as those calculated by FEM with acceptable deflections. As shown in Fig. 19, it is evident that DSIFs increase significantly with the increase of crack lengths.

5.3 A rectangular plate with three inner cracks

Fig. 20 shows a triple inner cracked rectangular plate. A suddenly imposed uniform tensile load $\sigma(t)$ is applied at the top surface of the plate. The load function is the same as that in Example 1. The size of plate is 20 mm × 40 mm. As shown in Fig. 20, a central horizontal crack CD with a length of 10 mm and two inclined cracks AB and EF with lengths of $2a$ are distributed in the plate.

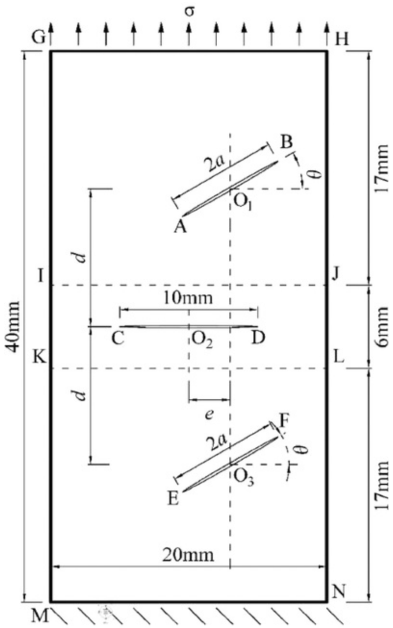

Fig. 20 A rectangular plate with three inner cracks.

alt-text: Fig 20

The frequencies and DSIFs with different crack lengths and crack angles are calculated. The vertical distance and the horizontal distance from the midpoints of two inclined cracks to the midpoint of the horizontal crack, as shown in Fig. 20, are fixed as $d = 10$ mm and $e = 0$ mm, respectively. Firstly, crack length $2a$ is taken to be 10 mm and the crack angle θ varies from 15° to 45°. Then, the crack angle is fixed as 45° and the crack length varies from 4 mm to 8 mm.

SFBEM based on the Erdogan fundamental solutions is used to calculate DSIF values. The plate is divided into three single inner cracked subdomains. In subdomains Ω_1 and Ω_3, 36 fictitious boundary elements and 72 boundary segments are adopted, and the distance between the fictitious boundary and the real boundary is taken to be 1 mm. Besides, in subdomain Ω_2, 28 fictitious boundary elements and 56 boundary segments are adopted, and the distance between the fictitious boundary and the real boundary is also taken to be 1 mm, as shown in Fig. 21. The cell numbers of 204, 218 and 228 are used for 15°, 30° and 45° of θ, respectively, whilst 228, 228 and 228 cells are used for 4 mm, 6 mm and 8 mm of $2a$, respectively. For all numerical integrations along the boundary, 5 Gauss points are used. The frequencies of the first six orders with different crack angles and crack lengths are shown in Table 6. K_{I} and K_{II} of crack tip B obtained with different crack angles and crack lengths are present in Figs. 22 and 23, while K_{I} of crack tip D obtained with different crack angles and crack lengths are present in Figs. 24 and 25.

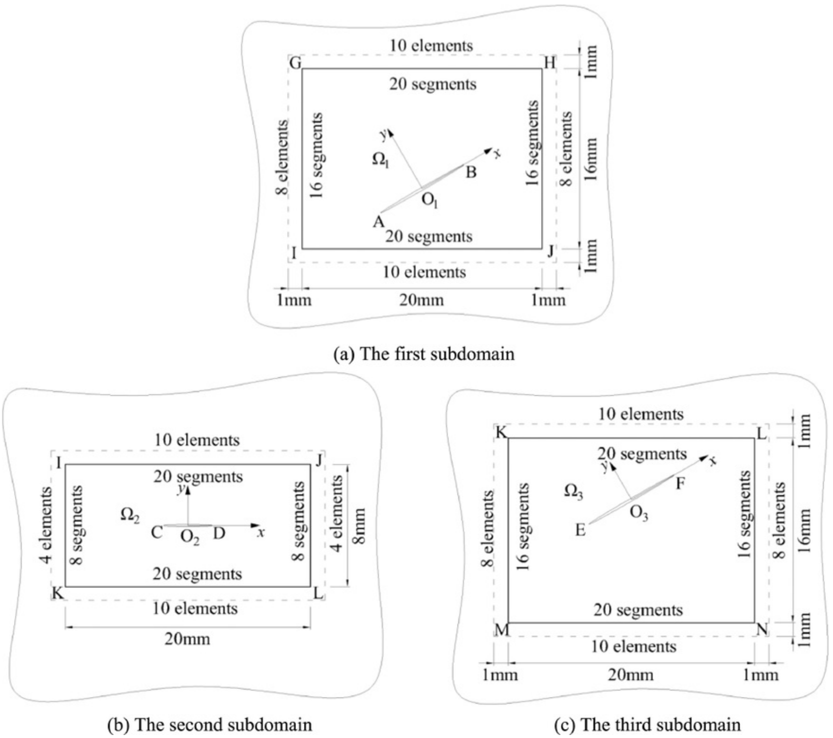

Fig. 21 Computational models for the triple inner cracked subdomain.

alt-text: Fig 21

Table 6 The frequencies of the first six orders with different crack angles and crack lengths (rad/s).

alt-text: Table 6

Order	2a=10 mm			θ=45°		
	θ=15°	θ=30°	θ=45°	2a=4 mm	2a=6 mm	2a=8 mm
1	49815.5	50709.5	51946.1	52423.0	52109.2	51954.9
2	157681.7	160958.2	168333.1	176006.8	174359.2	171931.8
3	192459.4	192834.9	193823.4	205937.2	202843.9	198698.2
4	399985.5	398913.9	395044.5	402325.7	401603.8	399517.7
5	421906.6	431148.5	435026.6	501857.2	495184.3	476882.1
6	475126.3	459816.5	469106.8	531681.3	507724.0	481073.9

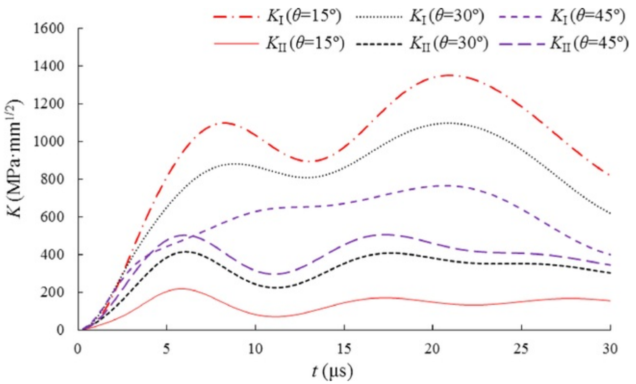

Fig. 22 **(Shrink the figure so as to fit one column in the PageProof.)** K_{I} and K_{II} of the crack tip B obtained with different crack angles.

alt-text: Fig 22

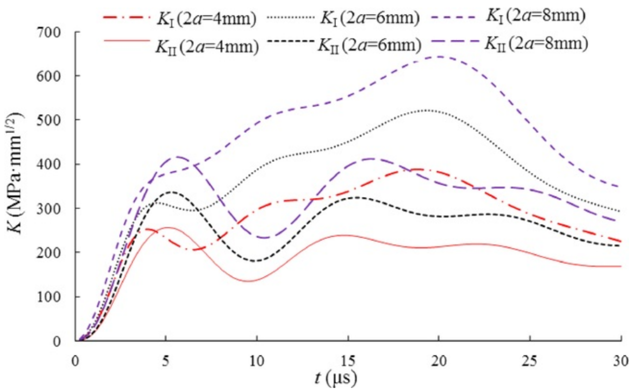

Fig. 23 **(Shrink the figure so as to fit one column in the PageProof.)** K_{I} and K_{II} of the crack tip B obtained with different crack lengths.

alt-text: Fig 23

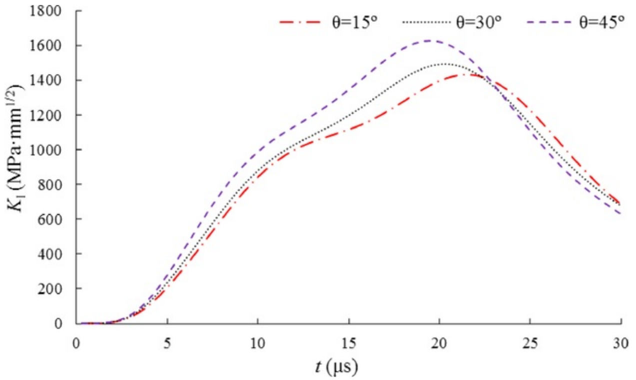

Fig. 24 **(Shrink the figure so as to fit one column in the PageProof.)** K_{I} of the crack tip D obtained with different crack angles.

alt-text: Fig 24

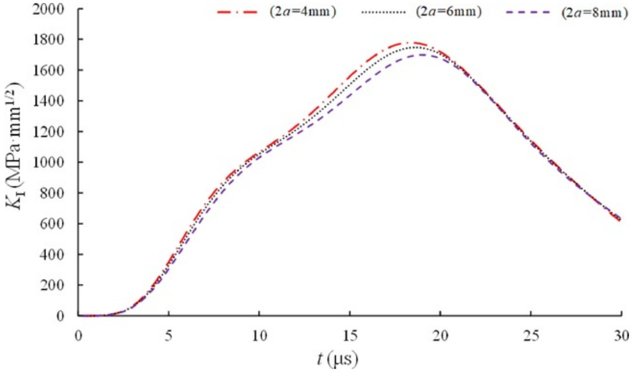

Fig. 25 **(Shrink the figure so as to fit one column in the PageProof.)** K_I of the crack tip D obtained with different crack lengths.

alt-text: Fig 25

From Table 6, it can be seen that the values of frequencies with the crack length of 10 mm are significantly smaller than those with the crack length of 4 mm, indicating that the appearance of cracks reduces the stiffness of the plate.

The results in Fig. 22 show that the values of K_I decrease with the increase of crack angle, and the curve associated with the crack angle of 15° has the largest fluctuation. Meanwhile, the values of K_{II} increase with the increase of crack angles. The results in Fig. 23 show that the values of K_I and K_{II} increase with the increase of crack lengths. It is worth mentioning that the results in both figures indicate that there is no obvious correlation between the K_I curve and the K_{II} curve. It can be seen from Figs. 24 and 25 that the K_I values of the central crack CD decrease with the decrease of crack angle and the increase of crack length. This is due to the shielding effect [22] of the lower and upper cracks.

The influence of the position of two inclined cracks is further investigated. Let the crack angle and crack length be θ=0° and 2a=8 mm, respectively. Firstly, the vertical distance d is fixed as 8 mm and the horizontal distance e varies from −2 mm to 2 mm. Then, the horizontal distance e is fixed as 4 mm and the vertical distance d varies from 6 mm to 14 mm. K_I values of crack tip D obtained under different horizontal distances are present in Fig. 26, while K_I values of the crack tip D obtained under different vertical distances are present in Fig. 27.

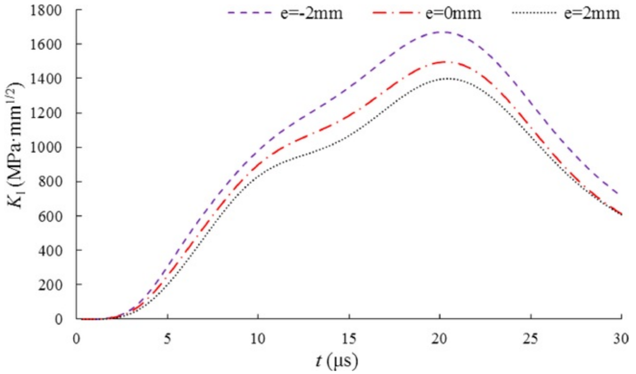

Fig. 26 **(Shrink the figure so as to fit one column in the PageProof.)** K_I of the crack tip D obtained under different horizontal distances.

alt-text: Fig 26

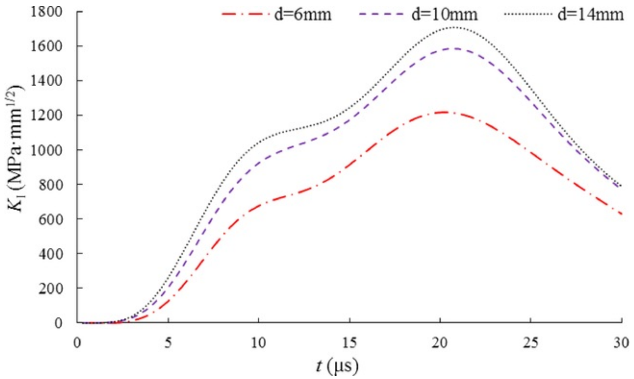

Fig. 27 **(Shrink the figure so as to fit one column in the PageProof.)** K_I of the crack tip D obtained under different vertical distances.

alt-text: Fig 27

From Fig. 26, it can be seen that when the upper and lower cracks move from the left side to the right side, i.e. close to the crack tip D, the values of K_I decrease clearly. From Fig. 27, one can see that when the vertical distance d decreases, i.e. close to the crack tip D, the values of K_I also show a large decrease, and the closer the crack is, the more obvious the decrease trend is. This indicates that the shielding effect [22] becomes larger with the decrease of the horizontal distance and the vertical distance.

6 Conclusions

The multi-domain SFBEM based on the Erdogan fundamental solutions is extended to dynamic analysis of multi-crack problems in this paper. Because of the use of the multi-domain coupling technique, the single crack Erdogan fundamental solutions have been shown to be applicable to the formulation of SFBEM for modal and transient analysis of the multi-crack problems. Moreover, the closed-form expressions of the strains are given in this research, so that the strain modes can be obtained directly and analytically. The fusion of the multi-domain SFBEM and the Erdogan fundamental solutions is computationally efficient, which provides a powerful tool for dynamic analysis of multi-crack problems. Numerical examples including the double inner crack, double edge crack and triple crack problems are analyzed in terms of the angular frequencies, the modal shapes and DSIFs by the present method. The convergence and accuracy of the proposed approach are studied in the first example for cracks with different inclined angles and lengths. In the second example, the plate with two edge cracks and subjected to the sine external loads is used to demonstrate the feasibility of the proposed approach. In the third example, the proposed method is used to study the interaction of three cracks on the dynamics characteristics of the plate.

Acknowledgements

The research is funded by the National Natural Science Foundation of China (51678252) and the Science and Technology Program of Guangzhou, China (201804020069).

References

[1] S.N. Atluri and T. Nishioka, Numerical studies in dynamic fracture mechanics, *Int J Fract* **27** (3–4), 1985, 245–261.

[2] D. Gross and T. Seelig, Dynamic fracture mechanics, 2011, Springer Berlin Heidelberg; Berlin.

[3] K. Kishimoto, S. Aoki and M. Sakata, Dynamic stress intensity factors using J-integral and finite element method, *Eng Fract Mech* **13** (2), 1980, 387–394.

[4] S.H. Song and G.H. Paulino, Dynamic stress intensity factors for homogeneous and smoothly heterogeneous materials using the interaction integral method, *Int J Solids Struct* **43** (16), 2006, 4830–4866.

[5] W.A. Yao, Z.Y. Cai and X.F. Hu, A new symplectic analytical singular element for crack problems under dynamic loading condition, *Eng Fract Mech* **188**, 2018, 431–447.

[6] T. Menouillard and T. Belytschko, Dynamic fracture with meshfree enriched XFEM, *Acta Mech* **213**, 2010, 53–69.

[7] T.Q. Bui and C.Z. Zhang, Analysis of generalized dynamic intensity factors of cracked magnetoelectroelastic solids by X-FEM, *Finite Elem Anal Des* **69**, 2013, 19–36.

[8] Z. Kang, T.Q. Bui and S. Hirose, Dynamic stationary crack analysis of isotropic solids and anisotropic composites by enhanced local enriched consecutive-interpolation elements, *Compos Struct* **180**, 2017, 221–233.

[9] P.H. Wen, M.H. Aliabadi and D.P. Rooke, Cracks in three dimensions: a dynamic dual boundary element analysis, *Comput Methods Appl Mech Eng* **167**, 1998, 139–151.

[10] C. Zhang, A. Savaidis, G. Savaidis and H. Zhu, Transient dynamic analysis of a cracked functionally graded material by a BIEM, *Comput Mater Sci* **26**, 2003, 167–174.

[11] A.S.M. Israil and G.F. Dargush, Dynamic fracture mechanics studies by time-domain BEM, *Eng Fract Mech* **39** (2), 1991, 315–328.

[12] P. Fedelinski, M.H. Aliabadi and D.P. Rooke, A single region time domain BEM for dynamic crack problems, *Int J Solids Struct* **32**, 1995, 3555–3571.

[13] D. Nardini and C.A. Brebbia, A new approach to free vibration analysis using boundary elements, *Appl Math Model* **7** (3), 1983, 157–162.

[14] P.H. Wen, M.H. Aliabadi and D.P. Rooke, A mass-matrix formulation for three-dimensional dynamic fracture mechanics, *Comput Methods Appl Mech Eng* **173**, 1999, 365–374.

[15] X.W. Gao, B.J. Zheng, K. Yang and C. Zhang, Radial integration BEM for dynamic coupled thermoelastic analysis under thermal shock loading, *Comput Struct* **158**, 2015, 140–147.

[16] Y.Y. Zhang and W. Feng, Investigation in weighted function and optimization of isoparametric singular boundary elements' size in 3-D crack problem, *Eng Fract Mech* **26**, 1987, 611–617.

[17] G.G. Luo and Y.Y. Zhang, Application of boundary element method with singular and isoparametric elements in three dimensional crack problems, *Eng Fract Mech* **29**, 1998, 97–106.

[18] F. Erdogan, On the stress distribution in plates with collinear cuts under arbitrary loads, In: *Proceedings of the fourth US national congress of applied mechanics,* 1962, 547–553.

[19] W. Tan P, S. Raju I and J. Newman, Boundary force method for analyzing two-dimensional cracked bodies, 1986, NASA Langley Research Center; Hampton.

[20] W.T. Ang, A boundary integral solution for the problem of multiple interacting cracks in an elastic material, *Int J Fract* **31**, 1986, 259–270.

[21] C. Su and C. Zheng, Probabilistic fracture mechanics analysis of linear-elastic cracked structures by spline fictitious boundary element method, *Eng Anal Bound Elem* **36** (12), 2012, 1828–1837.

[22] Z. Xu, C. Su and Z.W. Guan, Analysis of multi-crack problems by the spline fictitious boundary element method based on Erdogan fundamental solutions, *Acta Mech* **229** (8), 2018, 3257–3278.

[23] C. Su and D.J. Han, Multidomain SFBEM and its application in elastic plane problems, *J Eng Mech* **126**, 2000, 1057–1063.

[24] C. Su, S.W. Zhao and H.T. Ma, Reliability analysis of plane elasticity problems by stochastic spline fictitious boundary element method, *Eng Anal Bound Elem* **36**, 2012, 118–124.

[25] C. Su and J. Xu, Reliability analysis of reissner plate bending problems by stochastic spline fictitious boundary element method, *Eng Anal Bound Elem* **51**, 2015, 37–43.

[26] P.K. Banerjee and R. Butterfield, Boundary element methods in engineering science, 1981, McGraw-Hill; London.

[27] P.M. Prenter, Splines and variational methods, 2008, Courier Corporation; New York.

[28] D.Y. Zheng and N.J. Kessissoglou, Free vibration analysis of a cracked beam by finite element method, *J Sound Vib* **273** (3), 2004, 457–475.

[29] M. Kisa and M.A. Gurel, Modal analysis of multi-cracked beams with circular cross section, *Eng Fract Mech* **73** (8), 2006, 963–977.

[30] W.C. Ray and P. Joseph, Dynamics of structures, 2003, Computers & Structures Inc.; Berkeley.

Queries and Answers

Query: Please confirm that givennames and surnames have been identified correctly.
Answer: Yes

Query: Please verify figure 8.
Answer: Yes, it is correct.